

<https://doi.org/10.1038/s41524-024-01255-0>

Rotational magnetoelectric switching in orthorhombic multiferroics

Check for updates

Xu Li^{1,2}, Hao Tian³, Lan Chen^{1,2,4}, Hongjun Xiang⁵, Jun-Ming Liu¹, L. Bellaiche⁶, Di Wu^{1,2} & Yurong Yang^{1,2}

Controlling the direction of ferromagnetism and antiferromagnetism by an electric field in single-phase multiferroics will open the door to the next generation of devices for spintronics and electronics. The typical magnetoelectric coupling such as the linear magnetoelectric effect is very weak in type-I multiferroics and therefore the magnetoelectric switching is rarely achieved. Here, using first-principles simulations, we propose a magnetoelectric switching mechanism to achieve such highly desired control in orthorhombic multiferroics. One class of two-dimensional proper multiferroics (CrX_2Se_3 and MnX_2Te_3 , $X = \text{Sn, Ge}$) and perovskite multiferroics (EuTiO_3 and $\text{BiFeO}_3/\text{LaFeO}_3$ superlattice) are taken as examples to show the mechanism. In the ferroelectric switching process, the proper polarization rotates its direction by 180° and keeps its magnitude almost unchanged, the ferromagnetic or antiferromagnetic vector is rotationally switched by 180° following the rotation of ferroelectric polarization. This rotational magnetoelectric switching results from in-plane structural anisotropy and magnetic anisotropy, and the process of switching is governed by *cosine* functions from the phenomenological Landau-type models. This study addresses the challenge of magnetoelectric switching in type-I multiferroics by proposing a general magnetoelectric switching mechanism.

Magnetoelectric (ME) materials are experiencing great interest because of their inherent cross-coupling between electric and magnetic degrees of freedom^{1–4}. The systematic control of the magnitude and crystallographic direction of magnetic order parameters by an electric field is attractive for spintronics, next-generation memory devices, and other original devices. The first typical coupling between ferroelectric polarization (\mathbf{P}) and magnetic moment (\mathbf{M}) is via the existence of an energy term $\Delta E \sim P^2 M^2$ in some type-I multiferroics^{5–8}. The second typical ME coupling occurs in the type-II multiferroics, such as TbMnO_3 ^{9–11}, where the microscopic mechanism of polarization is connected with the spin-orbit interaction, via $\mathbf{P} \sim \mathbf{r}_{ij} \times [\mathbf{S}_i \times \mathbf{S}_j]$ (or other forms of energetic terms), where \mathbf{r}_{ij} is the vector connecting neighboring spins \mathbf{S}_i and \mathbf{S}_j ^{12–14}. The third typical ME coupling is an indirect coupling that occurs in the so-called hybrid improper multiferroics where two energy terms play a role, with the first involving the ferroelectric polarization and another structural parameter, and the second

term coupling this structural parameter with the magnetic order^{15–19}. However, these ME mechanisms still lack the achievement of practical potential applications based on them. The first typical ME coupling is weak and cannot reverse one ferroic parameter by switching the other ferroic degree of freedom. The second typical ME coupling occurs in type-II multiferroics which possess only very small polarization and usually possess multiferroicity only at low temperatures. The third typical ME mechanism exists in the hybrid improper ferroelectric materials, which are rare. Furthermore, most studies to describe the ME effect focus on the linear ME parameters which are usually very small^{20–26} and can not describe the complex ME switching process.

Here, we propose a ME mechanism of rotational switching magnetic vector by rotationally reversing the ferroelectric polarization from the first-principles calculations. The switching of both ferromagnetism^{27–30} and antiferromagnetism^{31–34} is investigated here, as the potential functional

¹National Laboratory of Solid State Microstructures and Collaborative Innovation Center of Advanced Microstructures, Nanjing University, Nanjing 210093, China.

²Jiangsu Key Laboratory of Artificial Functional Materials, Department of Materials Science and Engineering, Nanjing University, Nanjing 210093, China. ³School of Physics and Electronic Engineering, Zhengzhou Normal University, Zhengzhou 450044, China. ⁴School of Science, Nanjing University of Posts and Telecommunications, Nanjing 210023, China. ⁵Key Laboratory of Computational Physical Sciences (Ministry of Education), State Key Laboratory of Surface Physics, and Department of Physics, Fudan University, Shanghai 200433, China. ⁶Physics Department and Institute for Nanoscience and Engineering, University of Arkansas, Fayetteville, AR 72701, USA. ✉e-mail: chenlan@nju.edu.cn; diwu@nju.edu.cn; yangyr@nju.edu.cn

materials for spintronic applications. This ME coupling occurs in one class of orthorhombic two-dimensional (2D) proper multiferroics (CrX_2Se_3 and MnX_2Te_3 , $X = \text{Sn}, \text{Ge}$) and orthorhombic perovskite multiferroics (EuTiO_3 and $\text{BiFeO}_3/\text{LaFeO}_3$ superlattice). The in-plane ferroelectric polarization rotates from the $+P_a$ state to the $+P_b$ state, and then to the $-P_a$ state in the switching pathway, where the P_a state and P_b state are energetically degenerate, possess a polarization being perpendicular to each other and interchange their in-plane lattice constants. Because of structural and magnetic anisotropies, the magnetic vector rotates from \mathbf{a} to \mathbf{b} , and then to $-\mathbf{a}$ direction, following the rotation of the ferroelectric polarization. The rotational switching of ferroelectric polarization and magnetic vector can be described by a *cosine* function.

Results and discussion

Atomic structure of 2D CrX_2Se_3 and stability

First-principles method is used to study the structure, ferroelectric and magnetic properties, as well as the magnetoelectric coupling (see the details about Methods and Supplementary Information). It is important to recall that a variety of two-dimensional structures with various thicknesses from one atomic layer (graphene) to seven atomic layers (MA_2Z_4 family^{35,36}) and even up to nine atomic layers MXenes³⁷ has been recently discovered. In particular, two atomic layers 2D SnSe, GeSe, and SnTe adopt ferroelectric properties^{38–40}, while CrSe and MnTe possess (anti)ferromagnetic properties^{41,42}. It is thus legitimate to wonder if combining structures made by 2D ferroelectrics and (anti)ferromagnets could result in the formation of stable multiferroics^{43–45}. We indeed found one class of stable three-atom-layer 2D structures that are multiferroics, namely CrX_2Se_3 ($X = \text{Ge}, \text{Sn}$) and MnX_2Te_3 . CrX_2Se_3 possesses proper ferroelectric polarization and ferromagnetism, while MnX_2Te_3 exhibit proper polarization and anti-ferromagnetism. Various configurations of the three atomic layer structure are considered (see the detail in Supplementary Information). The most stable structure is such as the top and bottom layers are made of XSe (XTe) and the middle layer consists of CrSe (MnTe), as shown in Fig. 1, as well as Supplementary Table 4. Their resulting space group is $Pmm2$ with a point group of C_{2v} .

To investigate the stability of the 2D CrX_2Se_3 and MnX_2Te_3 ($X = \text{Ge}, \text{Sn}$), we first calculated the formation energy. The formation energy E_f is also calculated by $E_f = \frac{1}{6}(E_{\text{CrX}_2\text{Se}_3} - E_{\text{CrSe}} - 2E_{\text{XSe}})$, where $E_{\text{CrX}_2\text{Se}_3}$, E_{CrSe} , E_{XSe} are the energies in the formula unit of 2D CrX_2Se_3 , CrSe bulk⁴⁶ and XSe bulk^{47,48}, respectively, with $X = \text{Ge}, \text{Sn}$. Both orthorhombic (o- CrX_2Se_3) and hexagonal (h- CrX_2Se_3) structures are considered. The structures of CrX_2Se_3 , CrSe bulk, and XSe bulk can be found in Supplementary Fig. 3. As shown in Table 1, the formation energies of orthorhombic 2D structures of CrX_2Se_3 and MnX_2Te_3 ($X = \text{Ge}, \text{Sn}$) are in the range of 30–64 meV atom⁻¹, which is very similar or lower than those of experimentally stable VSe_2 and 2H-WS_2 . The small formation energies in our study thus indicate the stability of 2D structures of CrX_2Se_3 and MnX_2Te_3 ($X = \text{Ge}, \text{Sn}$). The structural stability is further evaluated by phonon spectrum and ab-initio molecular dynamics

calculations. The phonon spectrum of CrX_2Se_3 is shown in Supplementary Fig. 1. No significant imaginary frequency is found in the phonon dispersion, therefore confirming the dynamic stability of these compounds. We further performed ab-initio molecular dynamics (AIMD) calculations to study its stability under a high temperature of 600 K. As shown in Supplementary Fig. 2, both CrGe_2Se_3 and CrSn_2Se_3 are stable at high temperatures.

Spontaneous polarization and magnetism of 2D CrX_2Se_3

We first consider CrX_2Se_3 . The ferroelectric polarization of CrGe_2Se_3 and CrSn_2Se_3 are calculated to be $55 \mu\text{C cm}^{-2}$ and $26 \mu\text{C cm}^{-2}$ along \mathbf{a} direction, respectively (Here we use the effective thickness $3d/2$ to compute the polarization, because the distribution of electron cloud are considered), which are larger than or similar to that of prototypical ferroelectric BaTiO_3 ($26 \mu\text{C cm}^{-2}$)⁴⁹. The polarization comes from a polar mode (see Supplementary Fig. 5) and the 2D structures are proper ferroelectrics. The polarization mainly originates from the top and bottom XSe layers, the middle layer CrSe provides the ferromagnetism with $4 \mu_B$ on each Cr ion⁵⁰. Different magnetic configurations are considered, the ferromagnetic configuration is found to be the lowest energy state (see Supplementary Information for details) and thus the ground state. Magnetic anisotropy calculations shows that 2D CrX_2Se_3 possesses an easy axis along \mathbf{a} direction, which is parallel to the ferroelectric polarization.

In the 2D CrX_2Se_3 structures, each Cr ion in the middle layer has six nearest neighboring Se ions and is at the center of Se octahedra. There are three pairs of Cr-Se bonds along \mathbf{x} , \mathbf{y} , and \mathbf{z} direction, respectively, where \mathbf{x} is close to the direction of $\mathbf{a-b}$, \mathbf{y} is near $\mathbf{a+b}$, and \mathbf{z} is parallel to \mathbf{c} . The bonds for Cr_I (see Fig. 2) along the three directions are 2.7 Å, 3.2 Å, and 2.6 Å, respectively. This distortion expanding bonds along \mathbf{y} direction and shrinking bonds along the \mathbf{x} and \mathbf{z} direction are the Jahn-Teller one, which is induced by the e_g orbital splitting where $d_{3y^2-r^2}$ ($d_{3x^2-r^2}$) shifts to lower energy and is occupied, while $d_{z^2-x^2}$ ($d_{y^2-z^2}$) shifts to higher energy and is empty. Therefore three electrons of $3d^1$ occupy the three t_{2g} orbitals, and the fourth occupies $d_{3y^2-r^2}$ ($d_{3x^2-r^2}$). As shown in Fig. 2, the projected density of states (PDOS) displays occupations of $d_{3y^2-r^2}$ in Cr_I and $d_{3x^2-r^2}$ in Cr_{II} , indicating the orbital ordering of e_g between Cr_I and Cr_{II} . In the middle layer of the 2D structures, the interaction between Cr ions with 180° Cr-Se-Cr bond angle is the double exchange interaction, and that between Cr ions with about 90° Cr-Se-Cr bond angle is the well-known Goodenough-Kanamori-Anderson (GKA) superexchange interaction^{51–54}. The Jahn-Teller effect and corresponding orbit occupation result in a ferromagnetic exchange interaction in CrX_2Se_3 . In MnX_2Te_3 , there is no Jahn-Teller effect and an antiferromagnetic exchange interaction is energetically favorable.

The magnetic anisotropy properties

We now investigated the magnetocrystalline anisotropy energy (MAE). The MAE is a direction-related quantity which remains invariable for all symmetrical operations on the crystal (more details can be found in

Fig. 1 | Structures of 2D CrX_2Se_3 . **a** Side view of the structure with polarization along $+\mathbf{a}$ direction. **b–d** Top view of the structures with polarization along $-\mathbf{a}$, $+\mathbf{b}$ and $+\mathbf{a}$ direction, respectively. **e** The blue and red arrows represent the corresponding directions of \mathbf{P} and \mathbf{M} , respectively.

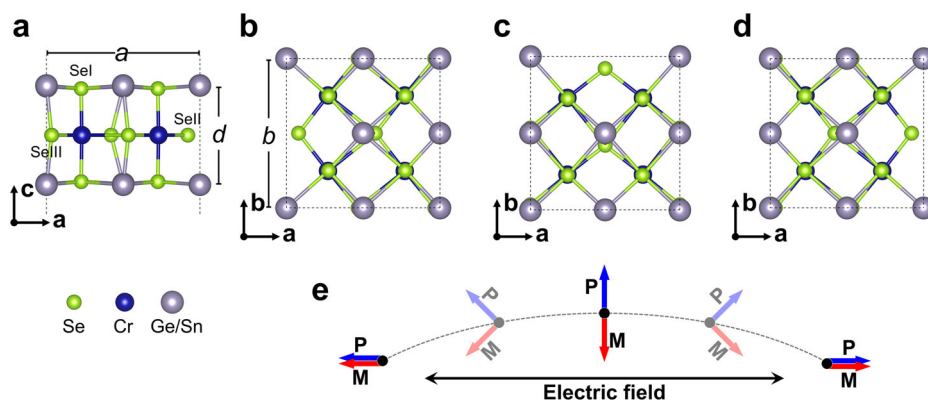


Table 1 | Formation energy

	o-CrGe ₂ Se ₃	o-CrSn ₂ Se ₃	h-CrGe ₂ Se ₃	h-CrSn ₂ Se ₃	VS ₂ ^{81,82}	2H-WS ₂ ^{49,83}
<i>E_f</i>	51.4	64.3	31.3	54.0	90	77

The calculated formation energy (meV atom⁻¹) of o-CrX₂Se₃ and h-CrX₂Se₃ (X = Ge, Sn). The formation energy of VS₂ and 2H-WS₂ are shown for comparison.

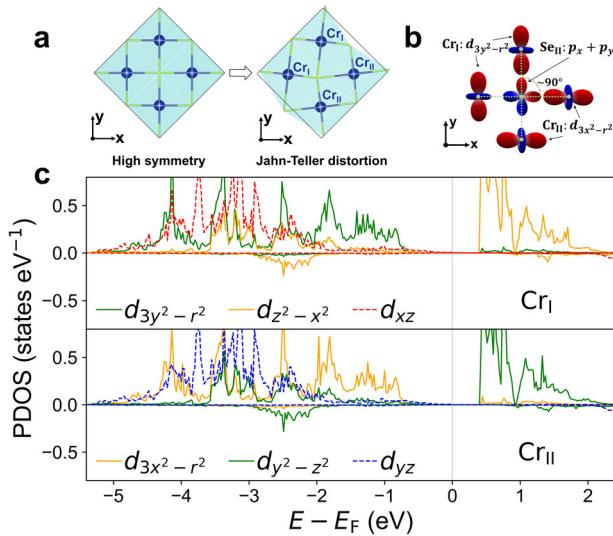


Fig. 2 | Jahn-Teller distortion in 2D CrX₂Se₃. **a** Jahn-Teller distortion of the middle atomic layer compared to the high symmetry structure. **b** The sketch of $d_{3x^2-r^2}$ and $d_{3y^2-r^2}$ orbitals of Cr ions. **c** PDOS of Cr_I and Cr_{II}.

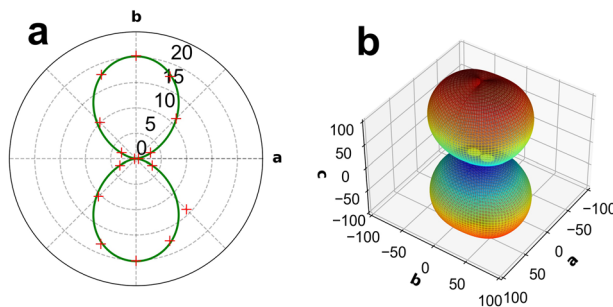


Fig. 3 | MAE (in $\mu\text{eV Cr}^{-1}$) of CrGe₂Se₃ as a function of the ferromagnetic direction. **a** MAE for ferromagnetic direction in the **ab** plane. **b** MAE for ferromagnetic direction in the three-dimensional space. The energy of ferromagnetic direction along the (**a**) direction is set to zero.

Supplementary Table 6). Based on the symmetry of C_{2v} and completeness of trigonometric polynomials, MAE can be expanded into trigonometric series as $\text{MAE}(\theta, \varphi) = \sum_{n,m} K_{nm} \sin^{2n}\theta \cos^{2m}\varphi$, where θ and φ are the azimuthal angle for **a** direction and polar angle for **c** direction, respectively, in the spherical coordinate system. K_{nm} are magnetocrystalline anisotropy parameters, and n and m are nonnegative integers. In most cases, the second order is enough to describe the phenomena of MAE and the higher orders can be neglected (Fig. 3, Supplementary Figs. 7 and 8). When neglecting terms of six and higher orders, MAE can be written as

$$\text{MAE} = E_0 + K_{10} \sin^2\theta + K_{01} \cos^2\varphi + K_{20} \sin^4\theta + K_{02} \cos^4\varphi + K_{11} \sin^2\theta \cos^2\varphi. \quad (1)$$

Based on this Eq. (1), MAE in the **ab** plane is $E_0 + K_{10} \sin^2\theta + K_{20} \sin^4\theta$. Figure 3a show the MAE of CrGe₂Se₃ for spins in the **ab** plane, which confirms that the phenomenological mode of Eq. (1) agrees very well with the first-principles calculations. The easy axis is along **a** direction and the energy difference between spins along **b** and **a** directions is about $20 \mu\text{eV Cr}^{-1}$. The calculations from both first principles and the model of Eq. (1) show that the MAE for a spin along the out-of-plane direction is larger than that along **a** direction by about $120 \mu\text{eV Cr}^{-1}$ (see the MAE in 3D space in Fig. 3b). CrSn₂Se₃ has the easy axis along **a** direction (see Supplementary Fig. 7).

Similar to CrX₂Se₃, MnX₂Te₃ are ferroelectric with polarization along **a** direction, and its magnitude is $49.2 \mu\text{C cm}^{-2}$ for $X = \text{Ge}$ and $50.5 \mu\text{C cm}^{-2}$ for $X = \text{Sn}$. MnX₂Te₃ possess the same point group of C_{2v} with CrX₂Se₃ and thus exhibit MAE that can be modeled by Eq. (1). The easy axis of MnX₂Te₃ is along **b** direction, therefore perpendicular to its polarization, which is thus different from the case of CrX₂Se₃ where both the easy axis and polarization are along **a** direction (see details in Supplementary Figs. 8 and 9).

Rotational magnetoelectric switching in 2D CrX₂Se₃

We then consider the switching of the ferroelectric polarization and magnetoelectric coupling. The energy barrier of the ferroelectric switching pathway is calculated from linearly changing the magnitude of polarization and also from the climbing-image solid-state nudged elastic band (ssNEB) method⁵⁵ which is particularly well-suited for ferroelectric switching due to its ability to accurately capture the energy landscape and transition pathways. As shown in Fig. 4a, the energy barrier from the ssNEB method is much smaller than that of linear changing polarization. In the switching pathway from ssNEB calculations, there are two maximal energy barriers of 83 meV f.u.^{-1} , and one minimal energy which is identical between the initial state +**P** and the final state -**P**. Figure 4c shows the polarization components of P_a along **a** and P_b along **b** direction. One can thus see that the polarization firstly is along +**a** direction at the reaction coordinate of 0, then rotates by 45° at the switching coordinate of 0.25, and rotates by 90° which is along +**b** direction at the switching coordinate of 0.50, then rotates by 135° at the coordinate of 0.75, and finally rotates by 180° which is along -**a** direction at the coordinate of 1.0. In this rotational switching of ferroelectric polarization, the polarization direction rotates by 180° from +**a** to -**a** and the magnitude of polarization is almost unchanged, rather different from the switching pathway where the polarization linearly changes and passes a zero polarization at the half of the pathway.

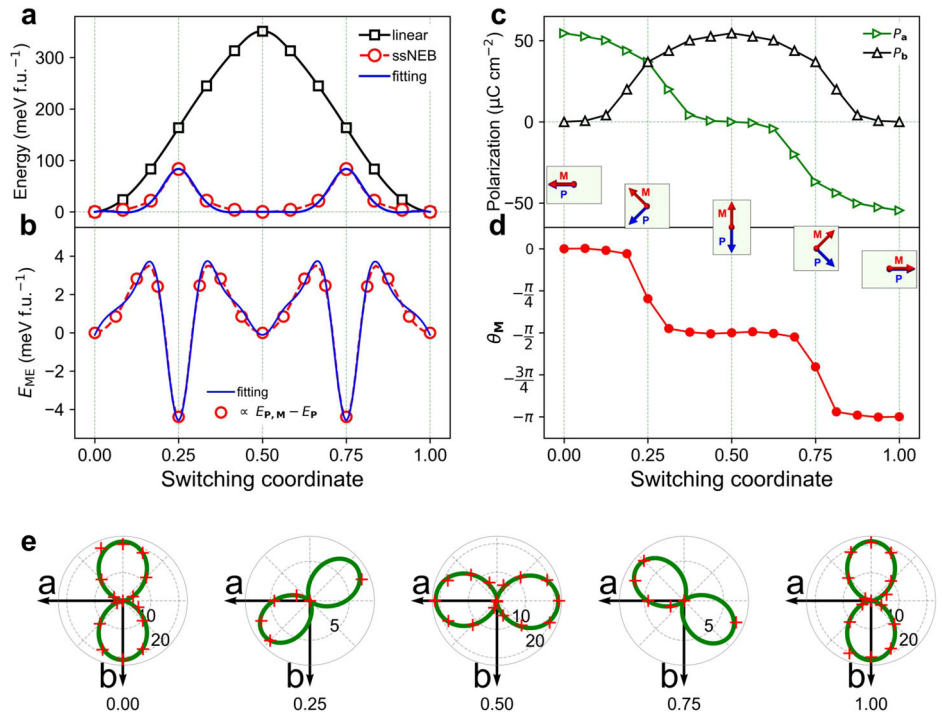
To understand the rotational switching ferroelectric polarization, we write the Landau free-energy potential as $E_P = \sum_{n,m} A_{nm} P_a^{2n} P_b^{2m}$, where A_{nm} is parameter, n and m are nonnegative integers. The magnitude of polarization slightly changes in the switching pathway, the free energy can be written as

$$E_P \sim A_{11} P_a^2 P_b^2 = A_{11} \frac{P^4}{8} [1 - \cos(4\theta_P)], \quad (2)$$

where θ_P is the angle between **P** and **a** direction, and $0^\circ \leq \theta_P \leq 180^\circ$. Therefore, the energy barrier in the rotational switching pathway is dependent on the direction of the polarizations in the switching process. Figure 4a confirms that the model of Eq. (2) agrees very well with the first-principles calculations.

The ferromagnetic vector (easy axis) of CrGe₂Se₃ also changes in the ferroelectric switching process. As the ferromagnetism along the out-of-plane direction has much higher energy than that in-plane direction by more than $120 \mu\text{eV f.u.}^{-1}$ (see Supplementary Fig. 3), the easy axis remains within the **ab** plane when switching the ferroelectric polarization. Figure 4e shows the in-plane MAE surface of a series of intermediate structures during the ferroelectric switching. One can see that the easy axis continuously rotates clockwise in the **ab** plane by 180° from **a** to -**a** (another possible path is from -**a** to **a** for the equivalent parallel/antiparallel magnetic vectors), during the switching of polarization. Figure 4d displays the evolution of angle (θ_M) between the easy axis and **a** direction in the switching pathway.

Fig. 4 | The evolution of physical quantities in the switching pathway. **a** The energy barrier of the ferroelectric switching pathway of CrGe₂Se₃ from state + **P** to state - **P** by ssNEB method and linearly changing the polarization. The blue line is the fitting by Eq. (2). **b** The energy difference between $E_{P,M}$ and E_P . The blue line is the fitting by Eq. (3). **c** Electrical polarization components along (a, b) directions. **d** The angle θ_M . **e** MAE (in $\mu\text{eV Cr}^{-1}$) in the **ab** plane. The switching coordinate of 0.0 and 1.0 represent + P_a and - P_a , respectively. The insets of the panel **c** and **d** are the sketches of the directions of **P** and **M** at the corresponding intermediate structures of the switching coordinate.



One can clearly see θ_M changes from 0 (at coordinate 0) to $-\pi/2$ (at coordinate 0.5), and then to $-\pi$ (at coordinate 1.0). The insets in Fig. 4c and d (also see Fig. 1e) also display the directions of ferromagnetism and polarization. This rotational switching of ferromagnetism originates from the magnetic anisotropy in the switching pathway (see Fig. 4e) where both lattice parameters and polarization are changed. For example, the initial state of + P_a has the lattice parameter $a = 8.45 \text{ \AA}$ and $b = 7.87 \text{ \AA}$, while the intermediate state of P_b (at the coordinate of 0.5) has the lattice parameter $a = 7.87 \text{ \AA}$ and $b = 8.45 \text{ \AA}$.

In the switching pathway, the easy axis M_e rotates clockwise by 180° and polarization **P** rotates anticlockwise by 180° (see Fig. 1e and the insets of Fig. 4c, d). To understand the rotational magnetoelectric switching, we determine the coupling between magnetism and polarization as

$$E_{ME} \propto -\alpha|\mathbf{P} \cdot \mathbf{M}_e|^2 - \beta|\mathbf{P} \times \mathbf{M}_e|^2 = -\alpha' - \beta' \cos(2\theta_{PM}), \quad (3)$$

where α and β are positive parameters, $\alpha' = (\alpha + \beta)P^2M^2/2$, $\beta' = (\alpha - \beta)P^2M^2/2$, P and M are the magnitudes polarization of and magnetic moment, respectively. P slightly changes and M remains the same during the switching pathway. θ_{PM} is the angle between **P** and M_e , and $0^\circ \leq \theta_{PM} \leq 360^\circ$. Note that the energy of magnetoelastic coupling is also included in Eq. (3). Figure 4b shows the energy difference between the calculations with spin-orbit coupling (SOC) ($E_{P,M}$ with magnetic vector) and without SOC (E_P without magnetic vector). The fitting of Eq. (3) agrees very well with the DFT calculations, indicating that **P** and M_e can be (anti)parallel or perpendicular to each other in the switching process. The lowest E_{ME} in Fig. 4b at coordinates 0.25 and 0.75 imply the largest magnetoelectric coupling during the switching, consistent with the fact that the very large response at the critical point of phase transition (the electrocaloric effect at Curie temperature⁵⁶⁻⁶¹, the piezoelectric effect at morphotropic phase boundaries^{62,63} and so on).

The phenomenon of ferromagnetism in CrGe₂Se₃ being switched by 180° by switching polarization under an electric field is also found in CrSn₂Se₃ (see Supplementary Fig. 12). The ferroelectric antiferromagnets of MnX₂Te₃ also exhibit rotational magnetoelectric switching phenomena (see Supplementary Figs. 13 and 14) which is confirmed by the calculation of polarization switching and antiferromagnetism switching under an external electric field (see Supplementary Figs. 15 and 16).

Rotational magnetoelectric switching in perovskites

The rotational magnetoelectric switching mechanism can be also found in other orthorhombic multiferroics. For instance, the prototypical orthorhombic multiferroic EuTiO₃^{28,64} and BiFeO₃/LaFeO₃ superlattice^{15,65}. We show the case of magnetoelectric switching of EuTiO₃ in Fig. 5. At tensile strain, EuTiO₃ exhibits ferromagnetic and ferroelectric properties. The ferroelectric polarization is along **a** direction and the easy axis is along **b** direction and the MAE is as large as $288 \mu\text{eV Eu}^{-1}$. As shown in Fig. 5a, the energy barrier for rotational ferroelectric switching is much lower than for linear ferroelectric switching. The ferroelectric switching energy fits Eq. (2) very well. As shown in Fig. 5d, the easy axis rotates gradually from $\pi/2$ to $-\pi/2$ when the ferroelectric polarization rotates from +**P** state to -**P** state. The energy surface of MAE shown in Fig. 5e also clearly exhibits the magnetization rotation in the ferroelectric switching pathway.

Note that the proposed ferroelectric and magnetoelectric switching mechanism is general in perovskite structures. To show the generality of the rotational switching, the ferroelectric switching of BaTiO₃ and magnetoelectric switching of BiFeO₃/LaFeO₃ are shown in Supplementary Figs. 17 and 18, respectively. The rotational ferroelectric switching in prototypical ferroelectric BaTiO₃, rather than the linear changing and reversing the polarization, further confirms the generality of the rotational switching mechanism.

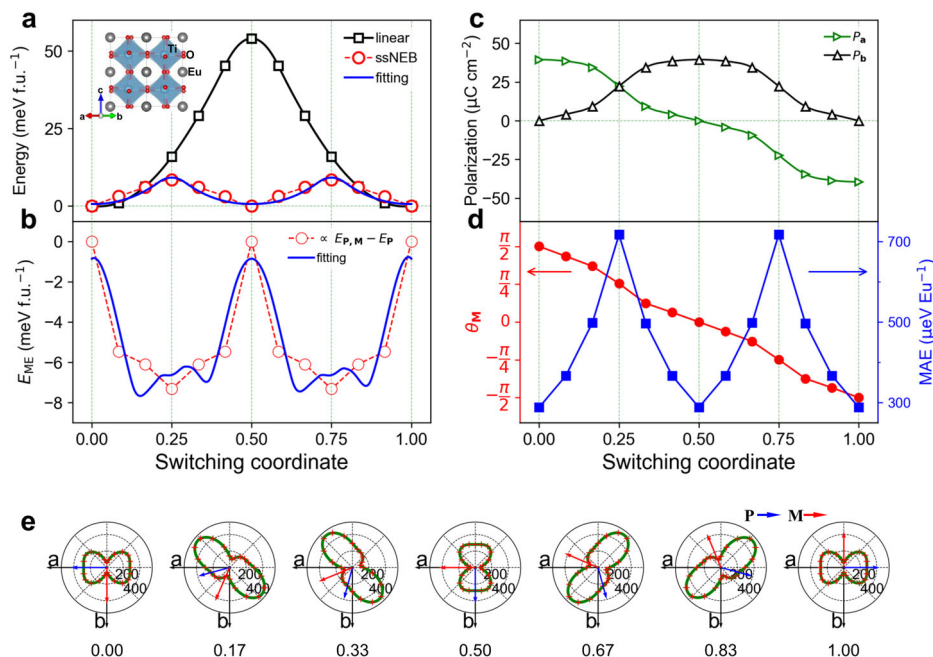
In summary, we propose a rotational magnetoelectric switching mechanism in two-dimensional multiferroics and perovskite multiferroics by first-principles methods. The orthorhombic structures possess strong structural and magnetic anisotropies. These strong anisotropies lead to the switching of proper polarization by rotating its direction by 180° , and result in the switching of (anti)ferromagnetism from rotating the magnetic vector by 180° . This magnetoelectric coupling mechanism opens a route to control spins by an electric field and broadens the potential application of spintronics. Note that this phenomenon may also occur in other structures with different symmetries⁶⁶.

Methods

Ab initio calculations

Density functional theory (DFT) calculations are performed with the Vienna Ab-initio Simulation Package (VASP)⁶⁷⁻⁶⁹, using the projected augmented wave (PAW) method⁷⁰ with the generalized gradient

Fig. 5 | The evolution of physical quantities in the ferroelectric switching pathway of EuTiO_3 under the epitaxial strain 2%. a The energy barrier of the ferroelectric switching pathway from state $+P$ to state $-P$ by ssNEB method and linearly changing the polarization. The blue line is fitting by Eq. (2). **b** The energy difference between $E_{P,M}$ and E_P . The blue line is fitting by Eq. (3). **c** Electrical polarization components along **a** and **b** directions. **d** The angle θ_M (red circles), and MAE (blue squares). **e** The energy surface of MAE in **ab** plane during the switching pathway. The blue and red arrows are the directions of **P** and **M**, respectively. The switching coordinate of 0.0 and 1.0 in the pathway represent $+P_a$ and $-P_a$, respectively. The inset of (a) shows the structure of EuTiO_3 under the epitaxial strain 2%.



approximation (GGA) parametrized by Perdew, Burke, and Ernzerhof (PBE) for the exchange-correlation functional⁷¹. The energy cutoff of 350 eV is adopted for the plane-wave basis sets. The Brillouin zone integration is sampled by using a Monkhorst-Pack **k**-point sampling with a mesh of $6 \times 6 \times 1$. A vacuum space larger than 15 Å was added along the out-of-plane direction to eliminate the interactions between replica artificial layers. The tolerance of 0.001 eV Å⁻¹ is used for the Hellman-Feynman forces during the atomic optimization and the convergence criterion for the energy is 10⁻⁷ eV. To account for the strongly correlated effect of the *d* orbit, an effective Hubbard value U_{eff} of 4.1 eV for Cr and 3.0 eV for Mn is used, as provided by the linear response approach⁷²⁻⁷⁴ and as also chosen when comparing with results from the HSE06 hybrid functional⁷⁵. The polarization was calculated using the Berry phase method⁷⁶. The phonon dispersion spectrum is calculated with the finite displacement method (Frozen-phonon approach)⁷⁷ on a $2 \times 2 \times 1$ supercell with 96 atoms by using the PHONOPY package⁷⁸. The climbing-image solid-state nudged elastic band (ssNEB) method was used for determining the ferroelectric switching paths and energy barrier⁷⁵. For the magnetocrystalline anisotropy energy calculations, a dense **k**-point mesh of $8 \times 8 \times 1$ and a more precise energy convergence criterion of 10⁻⁹ eV are used. The spin-orbit coupling (SOC) is included in the noncollinear magnetic calculations. The non-collinear calculations with SOC are all performed in a self-consistent manner. The electric field is applied by minimizing the approximate electric enthalpy^{8,19,79,80} (see the details in the Supplementary Information), which provides accurate results for the calculations in ferroelectric and multiferroic compounds. The supercell lattice and atomic position are relaxed to compute the energies of different magnetic configurations.

Data availability

The data supporting the findings of this study are available within this article and its Supplementary Information. Additional data that support the findings of this study are available from the corresponding author on reasonable requests.

Code availability

The VASP code used in this study is a commercial electronic structure modeling software, available from <https://www.vasp.at>. The in-house codes will be available from the corresponding authors upon reasonable request.

Received: 23 November 2023; Accepted: 22 March 2024;

Published online: 09 April 2024

References

- Spaldin, N. A. & Fiebig, M. The renaissance of magnetoelectric multiferroics. *Science* **309**, 391–392 (2005).
- Eerenstein, W., Mathur, N. D. & Scott, J. F. Multiferroic and magnetoelectric materials. *Nature* **442**, 759–765 (2006).
- Fiebig, M., Lottermoser, T., Meier, D. & Trassin, M. The evolution of multiferroics. *Nat. Rev. Mater.* **1**, 16046 (2016).
- Spaldin, N. A. & Ramesh, R. Advances in magnetoelectric multiferroics. *Nat. Mater.* **18**, 203–212 (2019).
- Smolenskii, G. A. & Chupis, I. E. Ferroelectromagnets. *Sov. Phys. Usp.* **25**, 475 (1982).
- Kimura, T. et al. Magnetocapacitance effect in multiferroic BiMnO_3 . *Phys. Rev. B* **67**, 180401(R) (2003).
- Palai, R., Scott, J. F. & Katiyar, R. S. Phonon spectroscopy near phase transition temperatures in multiferroic BiFeO_3 epitaxial thin films. *Phys. Rev. B* **81**, 024115 (2010).
- Xu, C. et al. Electric-field switching of magnetic topological charge in type-I multiferroics. *Phys. Rev. Lett.* **125**, 037203 (2020).
- Kimura, T. et al. Magnetic control of ferroelectric polarization. *Nature* **426**, 55–58 (2003).
- Kenzelmann, M. et al. Magnetic inversion symmetry breaking and ferroelectricity in TbMnO_3 . *Phys. Rev. Lett.* **95**, 087206 (2005).
- Kimura, T. Spiral Magnets as Magnetoelectrics. *Annu. Rev. Mater. Res.* **37**, 387–413 (2007).
- Katsura, H., Nagaosa, N. & Balatsky, A. V. Spin current and magnetoelectric effect in noncollinear magnets. *Phys. Rev. Lett.* **95**, 057205 (2005).
- Khomskii, D. Classifying multiferroics: Mechanisms and effects. *Physics* **2**, 20 (2009).
- Dong, S., Liu, J.-m., Cheong, S.-W. & Ren, Z. Multiferroic materials and magnetoelectric physics: Symmetry, entanglement, excitation, and topology. *Adv. Phys.* **64**, 519–626 (2015).
- Zanolli, Z., Wojdeł, J. C., Íñiguez, J. & Ghosez, P. Electric control of the magnetization in $\text{BiFeO}_3/\text{LaFeO}_3$ superlattices. *Phys. Rev. B* **88**, 060102(R) (2013).

16. Yang, Y., Íñiguez, J., Mao, A.-J. & Bellaiche, L. Prediction of a novel magnetoelectric switching mechanism in multiferroics. *Phys. Rev. Lett.* **112**, 057202 (2014).
17. Xu, B. et al. Hybrid improper ferroelectricity in multiferroic superlattices: Finite-temperature properties and electric-field-driven switching of polarization and magnetization. *Adv. Funct. Mater.* **25**, 3626–3633 (2015).
18. Lu, X. & Rondinelli, J. M. Room temperature electric-field control of magnetism in layered oxides with cation order. *Adv. Funct. Mater.* **27**, 1604312 (2017).
19. Chen, L. et al. Electric-field control of magnetization, Jahn-Teller distortion, and orbital ordering in ferroelectric ferromagnets. *Phys. Rev. Lett.* **122**, 247701 (2019).
20. Íñiguez, J. First-principles approach to lattice-mediated magnetoelectric effects. *Phys. Rev. Lett.* **101**, 117201 (2008).
21. Bousquet, E., Spaldin, N. A. & Delaney, K. T. Unexpectedly large electronic contribution to linear magnetoelectricity. *Phys. Rev. Lett.* **106**, 107202 (2011).
22. Bousquet, E. & Spaldin, N. Induced magnetoelectric response in *Pnma* perovskites. *Phys. Rev. Lett.* **107**, 197603 (2011).
23. Ye, M. & Vanderbilt, D. Dynamical magnetic charges and linear magnetoelectricity. *Phys. Rev. B* **89**, 064301 (2014).
24. Ye, M. & Vanderbilt, D. Magnetic charges and magnetoelectricity in hexagonal rare-earth manganites and ferrites. *Phys. Rev. B* **92**, 035107 (2015).
25. Ricci, F. & Bousquet, E. Unveiling the room-temperature magnetoelectricity of troilite FeS. *Phys. Rev. Lett.* **116**, 227601 (2016).
26. Tian, H., Bellaiche, L. & Yang, Y. Diversity of structural phases and resulting control of properties in brownmillerite oxides: A first-principles study. *Phys. Rev. B* **100**, 220103(R) (2019).
27. Gajek, M. et al. Spin filtering through ferromagnetic BiMnO₃ tunnel barriers. *Phys. Rev. B* **72**, 020406(R) (2005).
28. Lee, J. H. et al. A strong ferroelectric ferromagnet created by means of spin-lattice coupling. *Nature* **466**, 954–958 (2010).
29. Zhao, H. J. et al. Near room-temperature multiferroic materials with tunable ferromagnetic and electrical properties. *Nat. Commun.* **5**, 4021 (2014).
30. Bristowe, N. C., Varignon, J., Fontaine, D., Bousquet, E. & Ghosez, P. Ferromagnetism induced by entangled charge and orbital orderings in ferroelectric titanate perovskites. *Nat. Commun.* **6**, 6677 (2015).
31. Jungwirth, T., Marti, X., Wadley, P. & Wunderlich, J. Antiferromagnetic spintronics. *Nat. Nanotechnol.* **11**, 231–241 (2016).
32. Baltz, V. et al. Antiferromagnetic spintronics. *Rev. Mod. Phys.* **90**, 015005 (2018).
33. Gomonay, O., Baltz, V., Brataas, A. & Tserkovnyak, Y. Antiferromagnetic spin textures and dynamics. *Nat. Phys.* **14**, 213–216 (2018).
34. Chen, X. et al. Observation of the antiferromagnetic spin Hall effect. *Nat. Mater.* **20**, 800–804 (2021).
35. Hong, Y.-L. et al. Chemical vapor deposition of layered two-dimensional MoSi₂N₄ materials. *Science* **369**, 670–674 (2020).
36. Wang, L. et al. Intercalated architecture of MA₂Z₄ family layered van der Waals materials with emerging topological, magnetic and superconducting properties. *Nat. Commun.* **12**, 2361 (2021).
37. VahidMohammadi, A., Rosen, J. & Gogotsi, Y. The world of two-dimensional carbides and nitrides (MXenes). *Science* **372**, eabf1581 (2021).
38. Li, L. et al. Single-layer single-crystalline SnSe nanosheets. *J. Am. Chem. Soc.* **135**, 1213–1216 (2013).
39. Wu, M. & Zeng, X. C. Intrinsic ferroelasticity and/or multiferroicity in two-dimensional phosphorene and phosphorene analogues. *Nano Lett.* **16**, 3236–3241 (2016).
40. Wang, X. et al. Short-wave near-infrared linear dichroism of two-dimensional germanium selenide. *J. Am. Chem. Soc.* **139**, 14976–14982 (2017).
41. Zhang, Y. et al. Ultrathin magnetic 2D single-crystal CrSe. *Adv. Mater.* **31**, 1900056 (2019).
42. Li, B. et al. van der Waals epitaxial growth of air-stable CrSe₂ nanosheets with thickness-tunable magnetic order. *Nat. Mater.* **20**, 818–825 (2021).
43. Miao, N., Xu, B., Zhu, L., Zhou, J. & Sun, Z. 2D intrinsic ferromagnets from van der Waals antiferromagnets. *J. Am. Chem. Soc.* **140**, 2417–2420 (2018).
44. Jiao, J. et al. 2D magnetic Janus semiconductors with exotic structural and quantum-phase transitions. *J. Phys. Chem. Lett.* **10**, 3922–3928 (2019).
45. Miao, N. & Sun, Z. Computational design of two-dimensional magnetic materials. *WIREs Comput. Mol. Sci.* **12**, 1–21 (2022).
46. Corliss, L. M., Elliott, N., Hastings, J. M. & Sass, R. L. Magnetic structure of chromium selenide. *Phys. Rev.* **122**, 1402–1406 (1961).
47. Zhao, L.-D. et al. Ultralow thermal conductivity and high thermoelectric figure of merit in SnSe crystals. *Nature* **508**, 373–377 (2014).
48. Zhang, X. et al. Thermoelectric properties of GeSe. *J. Materiomics* **2**, 331–337 (2016).
49. Zhang, Y., Sun, J., Perdew, J. P. & Wu, X. Comparative first-principles studies of prototypical ferroelectric materials by LDA, GGA, and SCAN meta-GGA. *Phys. Rev. B* **96**, 035143 (2017).
50. Hill, N. A. Why are there so few magnetic ferroelectrics? *J. Phys. Chem. B* **104**, 6694–6709 (2000).
51. Anderson, P. W. Antiferromagnetism. Theory of superexchange interaction. *Phys. Rev.* **79**, 350–356 (1950).
52. Goodenough, J. B. Theory of the role of covalence in the perovskite-type manganites [La, M(II)]MnO₃. *Phys. Rev.* **100**, 564–573 (1955).
53. Kanamori, J. Superexchange interaction and symmetry properties of electron orbitals. *J. Phys. Chem. Solids* **10**, 87–98 (1959).
54. Huang, C. et al. Toward intrinsic room-temperature ferromagnetism in two-dimensional semiconductors. *J. Am. Chem. Soc.* **140**, 11519–11525 (2018).
55. Sheppard, D., Xiao, P., Chemelewski, W., Johnson, D. D. & Henkelman, G. A generalized solid-state nudged elastic band method. *J. Chem. Phys.* **136**, 074103 (2012).
56. Lisenkov, S. & Ponomareva, I. Intrinsic electrocaloric effect in ferroelectric alloys from atomistic simulations. *Phys. Rev. B* **80**, 140102(R) (2009).
57. Glazkova, E., Chang, C.-M., Lisenkov, S., Mani, B. K. & Ponomareva, I. Depolarizing field in ultrathin electrocalorics. *Phys. Rev. B* **92**, 064101 (2015).
58. Marathe, M., Grünebohm, A., Nishimatsu, T., Entel, P. & Ederer, C. First-principles-based calculation of the electrocaloric effect in BaTiO₃: A comparison of direct and indirect methods. *Phys. Rev. B* **93**, 054110 (2016).
59. Ma, Y.-B., Grünebohm, A., Meyer, K.-C., Albe, K. & Xu, B.-X. Positive and negative electrocaloric effect in BaTiO₃ in the presence of defect dipoles. *Phys. Rev. B* **94**, 094113 (2016).
60. Jiang, Z. et al. Giant electrocaloric response in the prototypical Pb(Mg, Nb)O₃ relaxor ferroelectric from atomistic simulations. *Phys. Rev. B* **97**, 104110 (2018).
61. Ma, X., Yang, Y., Bellaiche, L. & Wu, D. Large electrocaloric response via percolation of polar nanoregions. *Phys. Rev. B* **105**, 054104 (2022).
62. Bellaiche, L., García, A. & Vanderbilt, D. Low-temperature properties of Pb(Zr_{1-x}Ti_x)O₃ solid solutions near the morphotropic phase boundary. *Ferroelectrics* **266**, 41–56 (2002).
63. Bayara, T., Yang, Y., Ye, M. & Bellaiche, L. Giant linear magnetoelectric effect at the morphotropic phase boundary of epitaxial Sr_{0.5}Ba_{0.5}MnO₃. *Phys. Rev. B* **103**, L060103 (2021).
64. Yang, Y., Ren, W., Wang, D. & Bellaiche, L. Understanding and revisiting properties of EuTiO₃ bulk material and films from first principles. *Phys. Rev. Lett.* **109**, 267602 (2012).
65. Carcan, B. et al. Phase diagram of BiFeO₃/LaFeO₃ superlattices: Antiferroelectric-like state stability arising from strain effects and

- symmetry mismatch at heterointerfaces. *Adv. Mater. Inter.* **4**, 1601036 (2017).
66. Heron, J. T. et al. Deterministic switching of ferromagnetism at room temperature using an electric field. *Nature* **516**, 370–373 (2014).
 67. Kresse, G. & Hafner, J. Ab initio molecular dynamics for liquid metals. *Phys. Rev. B* **47**, 558–561 (1993).
 68. Kresse, G. & Furthmüller, J. Efficient iterative schemes for ab initio total-energy calculations using a plane-wave basis set. *Phys. Rev. B* **54**, 11169–11186 (1996).
 69. Kresse, G. & Furthmüller, J. Efficiency of ab-initio total energy calculations for metals and semiconductors using a plane-wave basis set. *Comput. Mater. Sci.* **6**, 15–50 (1996).
 70. Blöchl, P. E. Projector augmented-wave method. *Phys. Rev. B* **50**, 17953–17979 (1994).
 71. Perdew, J. P., Burke, K. & Ernzerhof, M. Generalized gradient approximation made simple. *Phys. Rev. Lett.* **77**, 3865–3868 (1996).
 72. Anisimov, V. I., Aryasetiawan, F. & Lichtenstein, A. I. First-principles calculations of the electronic structure and spectra of strongly correlated systems: The LDA + U method. *J. Phys.: Condens. Matter* **9**, 767–808 (1997).
 73. Dudarev, S. L., Botton, G. A., Savrasov, S. Y., Humphreys, C. J. & Sutton, A. P. Electron-energy-loss spectra and the structural stability of nickel oxide: An LSDA+U study. *Phys. Rev. B* **57**, 1505–1509 (1998).
 74. Cococcioni, M. & de Gironcoli, S. Linear response approach to the calculation of the effective interaction parameters in the LDA + U method. *Phys. Rev. B* **71**, 035105 (2005).
 75. Heyd, J., Scuseria, G. E. & Ernzerhof, M. Hybrid functionals based on a screened Coulomb potential. *J. Chem. Phys.* **118**, 8207–8215 (2003).
 76. King-Smith, R. D. & Vanderbilt, D. Theory of polarization of crystalline solids. *Phys. Rev. B* **47**, 1651–1654 (1993).
 77. Ackland, G. J., Warren, M. C. & Clark, S. J. Practical methods in ab initio lattice dynamics. *J. Phys.: Condens. Matter* **9**, 7861–7872 (1997).
 78. Togo, A. & Tanaka, I. First principles phonon calculations in materials science. *Scr. Mater.* **108**, 1–5 (2015).
 79. Fu, H. & Bellaiche, L. First-principles determination of electromechanical responses of solids under finite electric fields. *Phys. Rev. Lett.* **91**, 057601 (2003).
 80. Chen, L., Yang, Y. & Meng, X. K. Giant electric-field-induced strain in lead-free piezoelectric materials. *Sci. Rep.* **6**, 25346 (2016).
 81. Feng, J. et al. Metallic few-layered VS₂ ultrathin nanosheets: High two-dimensional conductivity for in-plane supercapacitors. *J. Am. Chem. Soc.* **133**, 17832–17838 (2011).
 82. Zhuang, H. L. & Hennig, R. G. Computational search for single-layer transition-metal dichalcogenide photocatalysts. *J. Phys. Chem. C* **117**, 20440–20445 (2013).
 83. Mahler, B., Hoepfner, V., Liao, K. & Ozin, G. A. Colloidal synthesis of 1T-WS₂ and 2H-WS₂ nanosheets: Applications for photocatalytic hydrogen evolution. *J. Am. Chem. Soc.* **136**, 14121–14127 (2014).

Acknowledgements

The authors thank the National Key R&D Program of China (Grants No. 2022YFB3807601 and No. 2020YFA0711504), the National Natural Science Foundation of China (Grants No. 12274201, No. 51721001, No. 12104416, and No. 52232001). L.B. thanks the Office of Naval Research (Grant No. N00014-21-1-2086), the Vannevar Bush Faculty Fellowship (VBFF) Grant No. N00014-20-1-2834 from the Department of Defense, and is thankful for support from the MonArk Quantum Foundry supported by the National Science Foundation Q-AMASE-i program under NSF Award No. DMR-1906383. We are grateful to the HPCC resources of Nanjing University for the calculations.

Author contributions

X.L. performed the first-principles calculations presented in this article with the help from H.T. and L.C. Y.Y., D.W., and L.C. supervised the project. X.L. and Y.Y. wrote the original manuscript. All authors contributed to the discussion of the project, results, and preparation of the manuscript.

Competing interests

The authors declare no competing interests.

Additional information

Supplementary information The online version contains supplementary material available at <https://doi.org/10.1038/s41524-024-01255-0>.

Correspondence and requests for materials should be addressed to Lan Chen, Di Wu or Yurong Yang.

Reprints and permissions information is available at <http://www.nature.com/reprints>

Publisher's note Springer Nature remains neutral with regard to jurisdictional claims in published maps and institutional affiliations.

Open Access This article is licensed under a Creative Commons Attribution 4.0 International License, which permits use, sharing, adaptation, distribution and reproduction in any medium or format, as long as you give appropriate credit to the original author(s) and the source, provide a link to the Creative Commons licence, and indicate if changes were made. The images or other third party material in this article are included in the article's Creative Commons licence, unless indicated otherwise in a credit line to the material. If material is not included in the article's Creative Commons licence and your intended use is not permitted by statutory regulation or exceeds the permitted use, you will need to obtain permission directly from the copyright holder. To view a copy of this licence, visit <http://creativecommons.org/licenses/by/4.0/>.

© The Author(s) 2024